Microorganism-Derived Heteroatom-Doped Carbon Materials for Oxygen Reduction and Supercapacitors

Hui Zhu, Jiao Yin, Xiaolei Wang, Hongyu Wang, and Xiurong Yang**

Heteroatom-doped carbon (HDC) has attracted tremendous attention due to its promising application in energy conversion and storage. Herein, due to its abundance high rate of reproduction, the microorganism, *Bacillus subtilis*, is selected as a precursor. An effective ionothermal process is adopted to produce the HDCs. Using acid activation, the obtained sample exhibits excellent electrocatalytic activity, long-term stability, and excellent resistance to crossover effects in oxygen reduction. Additionally, the base-treated sample exhibits superior performance in capacitors to most commercially available carbon materials. Even at a high current density, a relatively high capacitance is retained, indicating a great potential for direct application in energy storage.

1. Introduction

Heteroatom-doped carbon (HDC) has attracted tremendous attention due to its potential application in energy conversion and storage.[1] For example, such functional carbon materials have been considered as potential electrocatalysts for oxygen reduction reactions (ORR) to overcome the instinctive drawbacks of platinum-based catalysts (high cost, time dependent drift, and crossover deactivation).[2] On the other hand, eminent capacitive performance has been demonstrated via the cooperation of electrical double-layer capacitance (EDLC) and pseudocapacitance.[3] Meanwhile, considering the interfacial reactions, which are introduced by the heteroatom-containing functional groups, carbon materials with high surface areas will deliver improved performance. Up to now, several strategies, including in situ doping, post-treatment and direct pyrolysis, have been proposed to introduce heteroatoms into the matrix framework.[4–8] The in situ doping route involves the vapor decomposition of heteroatom enriched hydrocarbons over a metal catalyst (Fe, Co, Ni or Cu).[4] In the post-treatment procedure, the carbon matrix is subjected to a certain chemical environment (NH_3, urea, etc.) at a high temperature.[5] More recently, direct carbonization has emerged as a facile strategy without requiring the assistance of expensive instruments. To endow hierarchical structures and increase surface areas, several templates or carriers (SiO_2 nanoparticles, SBA-15, carbon, CNTs or graphene) are required, complicating the procedure and hindering the scale-up process.[6–8] Despite the methodology improvement, to lower the fabrication cost, the choice of precursor is an important consideration. In most cases, purified chemical agents or petroleum products are used as precursors. Thus, it is highly desirable but still an immense challenge to produce functional carbon with an efficient strategy from the cheap and renewable resources.[9,10]

Bacteria are a large group of prokaryotic microorganisms. They can replicate rapidly and persist in high numbers in almost any moist environment.[11] Despite their wide application in food and pharmaceutical industries, little attention has been paid to their role in material science. Detailed investigations have revealed that the bacterial cells consist of peptidoglycan, a polymer consisting of sugars and amino acids that forms a mesh-like layer outside the bacterial plasma membrane.[12] Considering the enriched heteroatoms, it is reasonable to question whether such microorganisms can be used as a convenient and renewable source to functionalize carbon. On the basis of it high worldwide abundance and fast rate of replication,[11,12] *Bacillus subtilis*, a Gram-positive model microorganism for laboratory studies, was adopted as the precursor.

2. Results and Discussion

Systematic characterization revealed the elliptical or rod-like morphology of the bacteria (1–2 μm, Figure S1a, Supporting Information) and the abundance of heteroatoms (EDX, Figure S1b, atomic ratio: C 64.91%, N 10.05%, O 14.1% and inorganic salts (Mg, Na, and K)). The abundance of heteroatoms implies that such microorganisms might be suitable HDC precursors.

To introduce porosity into the framework, a simple ionothermal method, which is effective in fabricating porous polymers,[13] was adopted. Different from the traditional activation route,[14] high-temperature pretreatment and pulverization were omitted in this procedure, which simplified the preparation and reduced energy consumption. In a typical synthesis, zinc chloride ($ZnCl_2$) or potassium hydroxide (KOH), a typical Lewis acid/base pair, were selected as activation agents and heating media (see the Experimental Section). The obtained samples were referred to as BZ-800 ($ZnCl_2$, 800 °C) and BP-800

Dr. H. Zhu, J. Yin, X. L. Wang, Prof. H. Y. Wang, Prof. X. R. Yang
State Key Laboratory of Electroanalytical Chemistry
Changchun Institute of Applied Chemistry
Chinese Academy of Sciences
Changchun, Jilin 130022, China
E-mail: hongyuwang@ciac.jl.cn; xryang@ciac.jl.cn

DOI: 10.1002/adfm.201201643

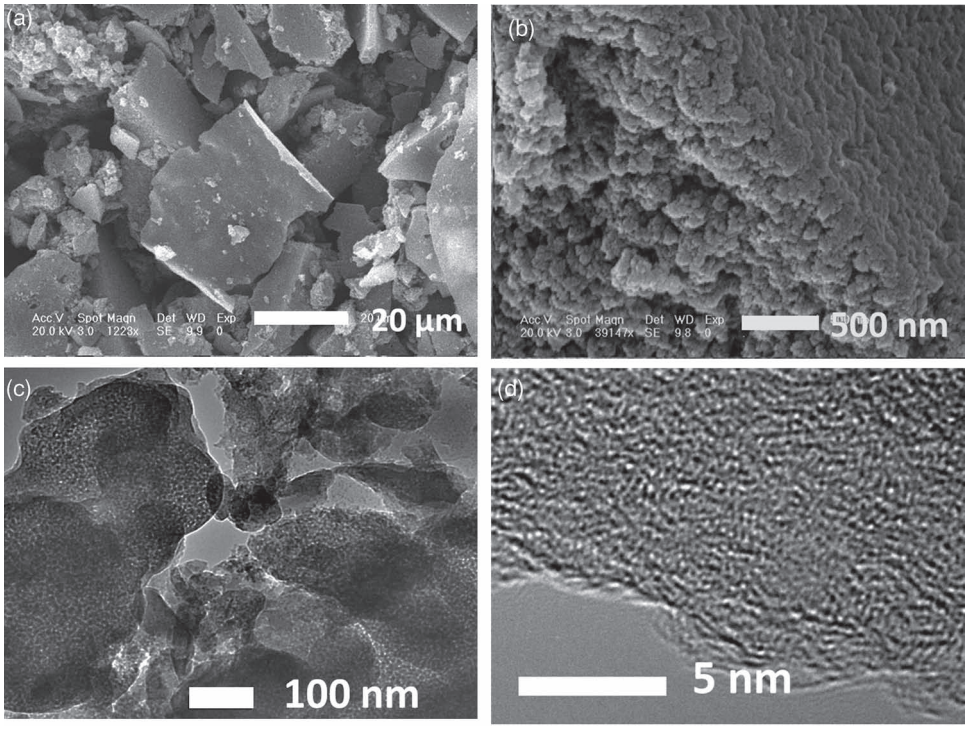

Figure 1. a,b) SEM, c) TEM, and d) HRTEM images of BZ-800; e) SEM and f) HRTEM images of BP-800.

(KOH, 800 °C), respectively. In addition, the direct carbonized sample (B-800) with a yield of 20% (weight percentage) was used for comparison. It was observed that the product yields varied in weight percentage with the heating media (BZ-800: 31%, BP-800: 15%), accordant with their different roles in tar formation and carbon gasification.[15] In another control, the commonly-used hydrothermal strategy was also conducted at 180 °C for 6 h (HT-B).[9,10] It was observed that the properties of the heating media had a great effect on the heteroatom doping nature as well as their correlative applications.

Representative scanning electron microscopy (SEM) images for BZ-800 are presented (**Figure 1**a). In contrast to their original elliptical morphology (Figure S1), bulk aggregations are observed for BZ-800. A closer observation reveals their secondary structures which are composed of nanometer-sized spherical particles (Figure 1b). Further detailed structural information was obtained by transmission electron microscopy (TEM). As shown in Figure 1c, spherical particles are intercalated with disordered, network-like interstitial pores. Many nanopores are observed in the magnified image (Figure 1d). Similarly, bulk aggregations of assembled subunits are also displayed for BP-800 (Figure 1e and Figure S2a). In addition, micropore-decorated defined structures are also confirmed for BP-800 (Figure 1f). In the control, HT-B and B-800 present the elliptical or rod-like morphologies (Figure S2b,c), in which the relatively smooth surface determined their poor porosity. Therefore, considering the discrepancies in morphology, it is deduced that the ionothermal method benefits the pulverization of bacteria and creates pores in the framework, which would increase surface areas and pore volumes.

To further investigate the reaction, N_2 sorption isothermal analysis was conducted (**Figure 2**a). It is observed that B-800 presents a type IV sorption isotherm with a BET surface area of 95.6 m^2 g^{-1}. In addition, a weak type H2 hysteresis loop is found, which might result from the interstitial porosity (Figure S2d). Comparatively, BZ-800 exhibits a combined type-I/IV sorption isotherm. Besides the microporous sorption at low pressure, the type H4 hysteresis loop proves the presence of mesopores in BZ-800. BP-800 displays a type I sorption isotherm, which is the characteristic of a microporous structure ($d \leq 2$ nm). The high N_2 sorption capacities imply their high surface areas and pore volumes (**Table 1**, BZ-800 and BP-800). Furthermore, the pore size distribution curves derived from the adsorption branch of the isotherms using nonlocal density functional theory (NLDFT) method are presented in Figure 2b. The B-800 sample shows almost no porosity, having a very low N_2 sorption pore volume, while the activated samples (especially BP-800) exhibit micropore formation as well as high microporous volumes. Compared with the nonporous characteristics of the raw bacteria (B) and HT-800 (Figure S3), it is concluded that the selection of heating media has a great effect on pore creation.

To confirm the chemical composition, X-ray photoelectron spectroscopy (XPS) and elemental analysis were conducted (**Figure 3**, Figure S4–6). As shown in Figure S4, three typical peaks corresponding to the binding energies of C 1s, N 1s, and O 1s are observed in the wide XPS survey scan for BZ-800. In contrast to BZ-800, the N1s peak is weak in BP-800 (Figure 3e, Figure S4). This discrepancy is in accordance with the previous observation that the nitrogen functional groups are easy

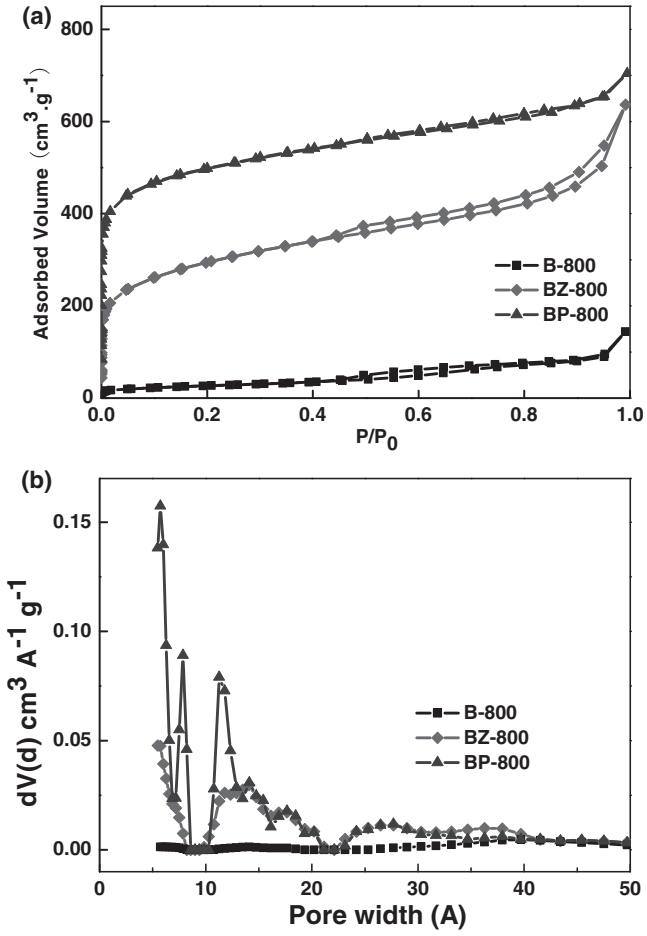

Figure 2. a) N_2 sorption isotherms and b) NLDFT pore size distributions of samples (B-800, BZ-800, and BP-800).

to oxidatize, especially in basic media.[9c,15] The absence of any other peaks in the pattern clearly indicates the complete removal of metal traces. In control, a high doping level of oxygen and nitrogen is found for B-800 (Figure S4). In addition, a small amount of phosphorus is also retained in B-800. Quantitative analysis elucidates the corresponding atom contents (BZ-800: C-88.2%, O-7.1%, N-4.7%; BP-800: C-82.9%, O-16.4%, N-0.7%; Table 1), consistent with both the molar composition derived from elemental analysis (B-800: $C_1N_{0.04}O_{0.18}H_{0.43}$, BZ-800: $C_1N_{0.08}O_{0.24}H_{0.24}$, BP-800: $C_1N_{0.01}O_{0.50}H_{0.88}$, Table 1) and the EDX data (Figure S7). Therefore, it is concluded that the heating media also affects the composition in the framework.

Catalysts for ORR are at the heart of key renewable-energy technologies including fuel cells and metal-air batteries.[16] The ORR can proceed either through a four-electron process to directly combine oxygen with electrons and protons into water as the end product, or a less efficient two-step, two-electron pathway involving the formation of hydroperoxide ions as intermediates.[17] To assess the catalytic activity of our samples, cyclic voltammetry (CV) was performed (Figure S8). Compared with their featureless character in N_2 saturated solution (0.1 M KOH), catalytic peaks are found in O_2 saturated solutions, indicating certain catalytic activity towards ORR. Typically, a cathodic peak located at –0.28 V is found for BZ-800 (Figure S8d). This value is positively shifted about 160 mV compared to the bare glassy carbon electrode (Figure S8a, –0.44 V),[6,7] indicating an excellent catalytic ability for the ORR. To gain dynamitic information, the electrocatalytic abilities were evaluated from rotating ring-disk electrode (RRDE) voltammograms (**Figure 4**a). The onset potential of the other two samples (B-800: –0.12 V, BP-800: –0.18 V) shift negatively compared with that of BZ-800 (–0.06 V), consistent with the deduction from Figure S8. The cathodic current densities also decrease to a certain extent. Furthermore, unlike the one-step process for BZ-800, a typical two-step ORR process is discovered for BP-800, which proves an indirect two-electron reduction of oxygen. We attribute this to the negligible content of nitrogen in BP-800. The transferred electron number per oxygen is calculated to be 3.93 for BZ-800, 3.66 for B-800, and 3.12 for BP-800, respectively.

To further understand the electorcatalytical activities heteroatoms in ORR, narrow scan N1s XPS spectra were analyzed. No typical nitrogen signal is observed for BP-800 (Figure 3e and Figure S4). In contrast, about 4–5 At% of nitrogen is detected for B-800 and BZ-800 (Table 1, Figure S4). The N 1s signals can be deconvoluted into 5 different types of nitrogen species: pyridinic (398.5 eV), nitrile or imine (399.5eV), pyrrolic (400.5 eV), graphitic (401.3 eV) nitrogen, and oxidized nitrogen (402–405 eV) (Figure 3b and Figure S5). Quantitative analysis reveals that high percentages of pyridinic, pyrrolic and graphitic types of nitrogen are contained in BZ-800 and B-800, which are thought to be responsible for the high activity. In addition, compared with the O 1s peak of BP-800 (Figure 3f), which can be ascribed to adsorbed oxygen (531.2 eV), =C=O/–C–O–C– (532.2 eV), –O–C=O (533.2 eV) respectively, several –N–O– (534.1 eV) functional groups are detected for BZ-800 (Figure 3c).[18] Interestingly, B-800 with high nitrogen content

Table 1. Chemical composition and textural characteristics of samples (bacteria, B-800, BZ-800, and BP-800).

Sample	S_{BET}[a] [$m^2\ g^{-1}$]	S_{mic}[b] [$m^2\ g^{-1}$]	S_{mes}[c] [$m^2\ g^{-1}$]	Pore Volumes [$cm^3\ g^{-1}$][d]	At%[e] C	At%[e] N	At%[e] O	Molar Composition[f]
Bacteria	6.43	0.0	6.43	0.011	64.9	10.1	14.1	–
B-800	95.6	0.0	95.6	0.224	84.3	3.73	11.4	$C_1N_{0.04}O_{0.18}H_{0.43}$
BZ-800	985	515	470	0.986	88.2	4.66	7.2	$C_1N_{0.08}O_{0.24}H_{0.24}$
BP-800	1578	1133	442	1.092	82.9	0.68	16.4	$C_1N_{0.01}O_{0.50}H_{0.88}$

[a]Specific surface area from multiple BET method; [b]Micropore surface area from t-plot method; [c]t-method external surface area ($S_{mes} = S_{BET}$-S_{mic}); [d]Total pore volume at $P/P_0 = 0.99$; [e]Atomic ratio data from XPS analyses; [f]Data from elemental analysis.

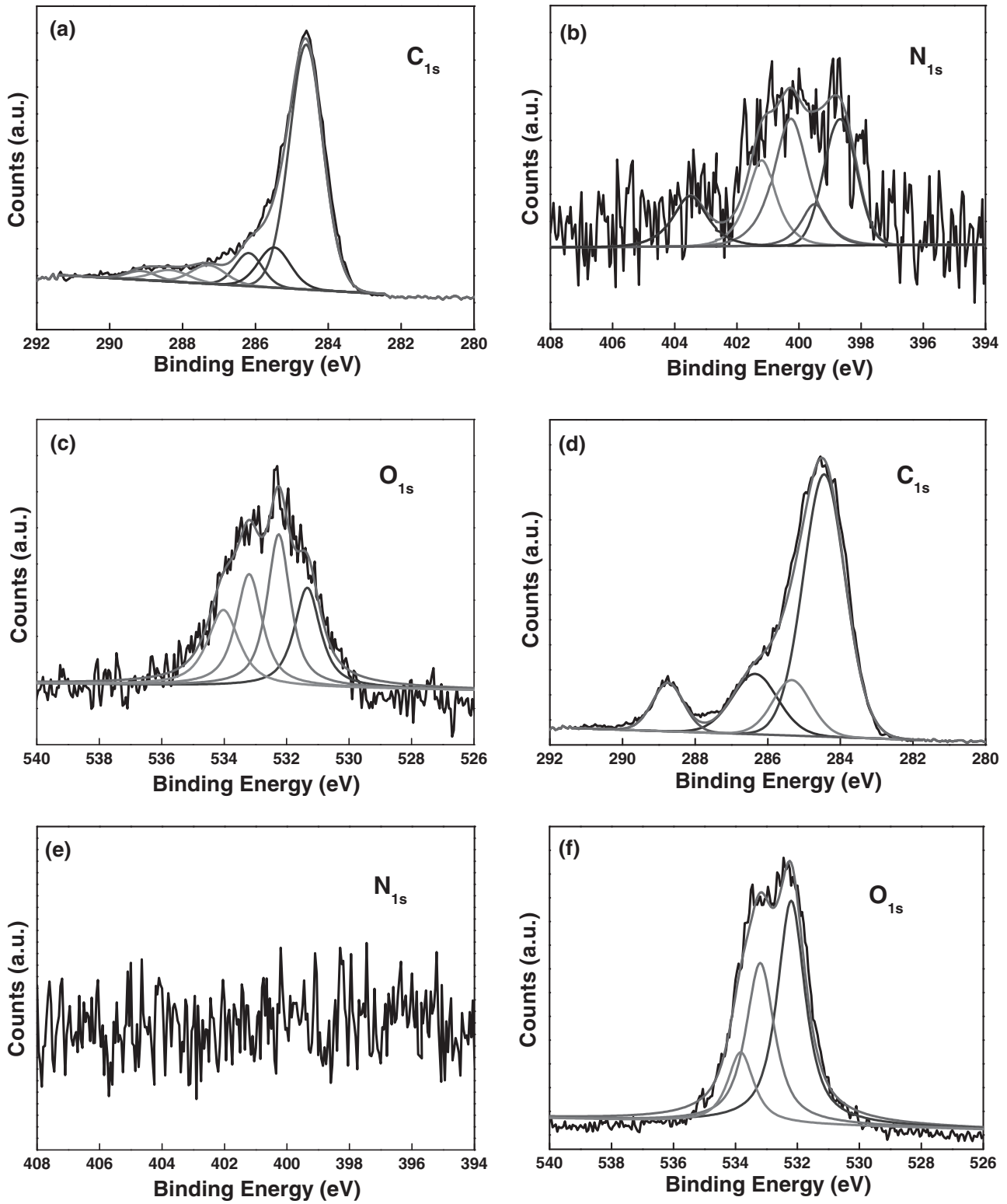

Figure 3. High resolution XPS scans of BZ-800: a) C1s; b) N1s; c) O1s; and BP-800: d) C1s; e) N1s; f) O1s.

shows the relatively low ORR activity. Considering its low surface area and almost nonporous structure (Figure 2 and Figure S3), this observation might result from the kinetic inaccessibility of O_2.[6] Therefore, we may deduce the final ORR electrocatalytic activities are simultaneously controlled by the nitrogen content and the porous architectures.

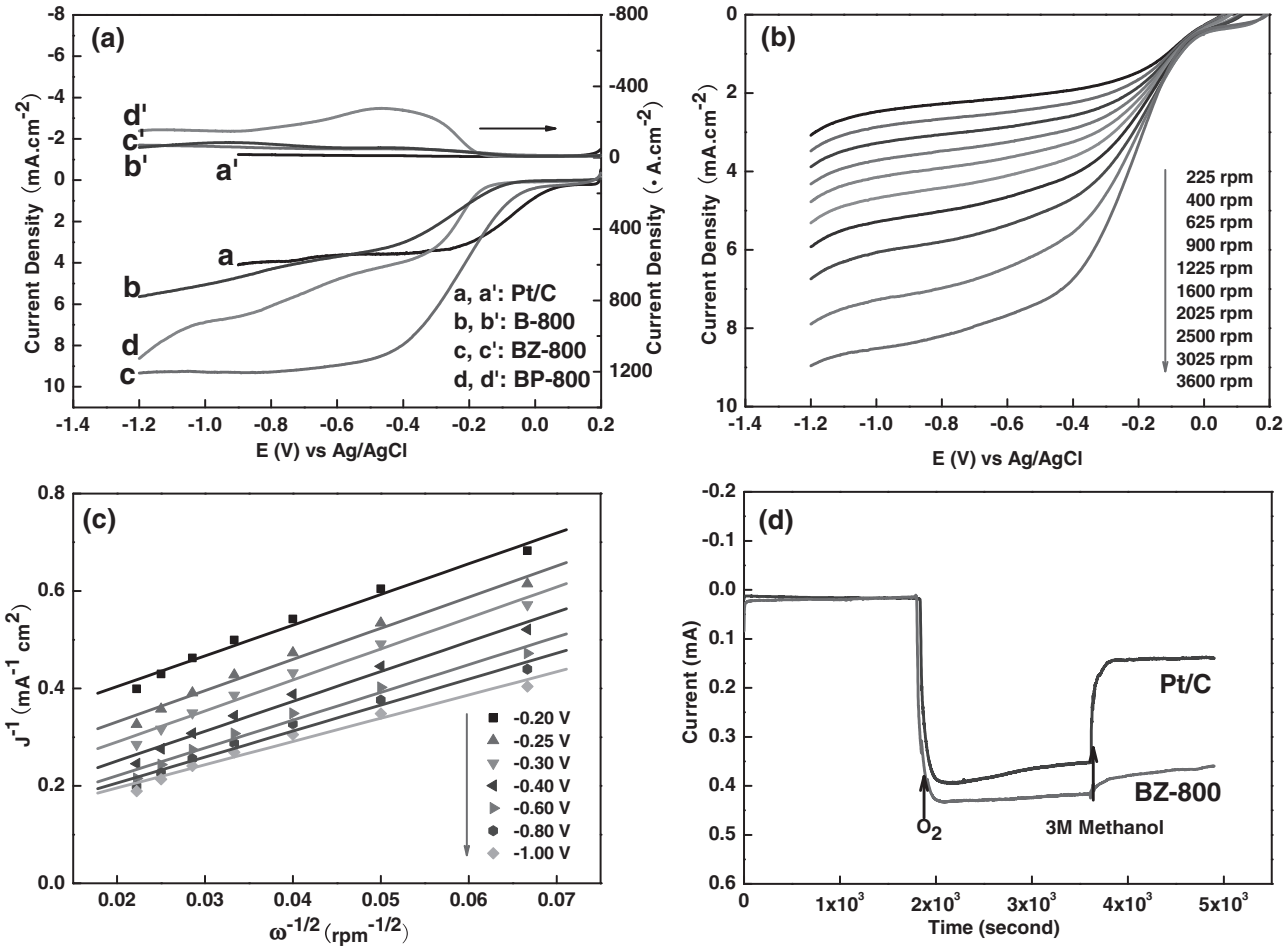

Figure 4. Electrocatalytic activity in ORR in 0.1 M KOH. a) RRDE voltammograms in O_2 saturated solution at a scan rate of 10 mV s^{-1}. (The electrode rotation rate was 3600 rpm) b) RDE voltammograms of BZ-800 in O_2 saturated solution at a scan rate of 10 mV s^{-1}, and at different rotation rates. c) Koutecky–Levich plot (J^{-1} vs $\omega^{-1/2}$) at different potentials. d) Current-time (*i–t*) response of BZ-800 and 20 wt% Pt/carbon at –0.30 V in 0.1 M KOH saturated with N_2 (0–1800 s) and O_2 (1800–3600 s) and in O_2-saturated 3 M CH_3OH (3600–4800 s).

To gain an insight into the action of BZ-800 during the ORR, the reaction kinetics were studied via rotating-disk voltammetry (RDE, Figure 4b). The current densities increase with rotation rates, due to the shortened diffusion layer. The corresponding Koutecky–Levich (K-L) plots at various potentials display good linearity (Figure 4c). The slopes remain approximately constant over the potential range from –0.2 to –0.8 V, implying similar electron transfer numbers for oxygen reduction at different potentials. Calculated from the K-L equation, the electron transfer numbers per oxygen molecule are close to 4 (3.96), suggesting that the ORR catalyzed by BZ-800 mainly follows the 4e reduction mechanism.[17] Remarkably enough, deduced from the slope and intercept of the K-L plots, BZ-800 exhibits a high kinetic current density of 48.0 mA cm^{-2} at –0.40 V. This value is twice that of commercially available Pt/C (20 wt% platinum on Vulcan XC-72R, J_k = 20 mA cm^{-2}). To further evaluate the stability/durability of BZ-800, the current-time (*i–t*) plots are presented (Figure 4d). The better stability of BZ-800 for ORR can be demonstrated from their negligible current decay, compared with that of Pt/C. Another advantage of BZ-800 over Pt/C is its prominent insensitivity to methanol. It is thought that such nitrogen-doped porous carbon (BZ-800) might be a promising candidate for ORR due to its high catalytic activity, stability and selectivity.

Besides utilization in oxygen reduction, heteroatom-doped carbon also plays an important role in energy storage. The doped atoms often contribute to the capacity improvement.[19–21] To evaluate the potential of our products, cyclic voltammetry was carried out with a three-electrode system (Figure S9). Different from the ideal EDLC behavior, distorted rectangular shapes emerge. Such a deviation might arise from the incorporated hetero-atoms into the carbon matrix.[22,23] Despite the high heteroatom content, the specific capacitance of B-800 is very low, which correlates with its low specific area (96 m^2 g^{-1}). This result reflects that all involved reactions are interface-bound, i.e., a significant surface area is necessary for obtaining high capacitive performance. In the presence of KOH or $ZnCl_2$, these carbons exhibit a surprisingly high capacitive performance as compared with the activated carbons with similar surface areas.[22] Among them, BP-800 presents the best performance

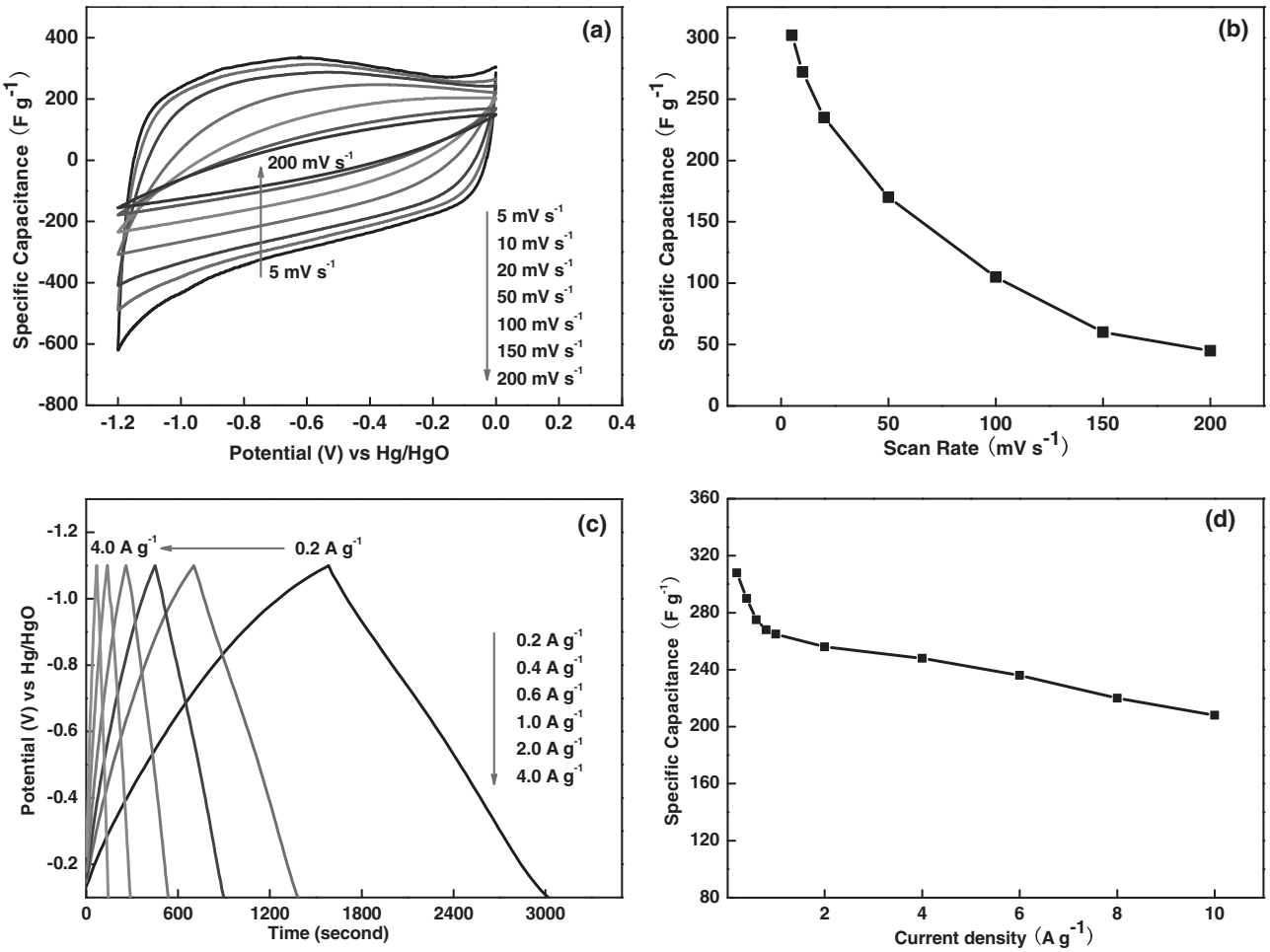

Figure 5. Electrochemical capacitive behavior of BP-800 in 6 M KOH. a) CVs at different scan rates. b) Variation of specific capacitance with scan rate. c) Galvanostatic charge/discharge curves with different current densities. d) Specific capacitance as a function of current density.

in both acid and basic electrolytes, due to its high surface area and heteroatomic abundance (**Figure 5** and Figure S10). As shown in Figure 5a,b, the estimated specific capacitance (SC) value decrease steadily with the increased scan rate from 5 to 200 mV s^{-1}, due to the confined microporous structure, which hinders the effective mass and charge transfer.[21,22]In addition, it is worthwhile of note that the typical capacitance enhancement at negative potentials indicates the easy adsorption/desorption of positively charged ions. Similar phenomena are observed in H_2SO_4 (Figure S10), as protons are preferably adsorbed at the electrode surface.[22,23]To further illuminate the role of doping in capacitive improvement, narrow scan C1s XPS spectra were analyzed (Figure 3d). Compared with BZ-800 and B-800 (Figure 3a and Figure S5), a broader C1s spectrum is observed for BP-800. After deconvolution, peaks located at 284.6, 285.5, 286.2, 287.4, and 288.8 eV are attributed to C=C (43%), C–C (31%), C–OR (13%), –C=O (11%), and –O–C=O (2%) groups respectively.[18] Taking the high surface area into account, it is deduced that the capacitive response comes from the cooperation of EDLC and oxygen-functionality-related pseudocapacitance of the material.

Finally, galvanostatic charge/discharge, which is considered as the most accurate characterization technique for redox capacitors, was performed in the potential window from –1.1 to –0.1 V to determine the capacitance dependence on current density. The small deviation from linearity demonstrates a pseudocapacitive contribution (Figure 5c). Combining the high surface area (1133 m^2 g^{-1}) and heteroatom doping level, the specific capacitance of BP-800 is 310 F g^{-1} in 6 M KOH and 305 F g^{-1} in 1 M H_2SO_4 at a current density of 0.2 A g^{-1} (Figure 5d and Figure S10d). These values are higher, compared with activated carbons with surface areas greater than 3000 m^2 g^{-1}.[9c,22] Even at a high current density of 10 A g^{-1}, a relative high capacitance of BP-800 is retained (200 F g^{-1} in 6 M KOH and 205 F g^{-1} in 1 M H_2SO_4). To validate their practical application, the cyclic stability of samples was examined by charge-discharge cycling. As shown in Figure S11, the specific capacitance of BP-800 slightly decreased during the first 50 cycles but was constant thereafter, still remaining at more than 96% after 1200 cycles. Thus, such a carbon material presents great potential in energy storage applications.

3. Conclusions

Heteroatom-doped carbon materials were successfully obtained from bacteria via an ionothermal process. The composition and porosity can be controlled with the selection of heating media. Excellent electrocatalytic activity towards the oxygen reduction reaction and high capacitance were demonstrated. To the best of our knowledge, this is the first time that both properties (electrocatalytic activity and capacitance) of a carbon material have been imbued from the same precursor.

4. Experimental Section

Synthesis: *Bacillus subtilis* (Hubei Qiming Bio Engineering Co. Ltd.) was used as the precursor. In a typical synthesis, after mixing bacteria with $ZnCl_2$ at a mass ratio of 1:4, the mixture precursor was carbonized in a tube furnace at 800 °C for 2 h under nitrogen flow. The obtained sample, referred to as BZ-800, was subsequently washed in 2 M HCl and distilled water to remove any metal residue. The BP-800 sample was obtained via a similar procedure with the substitution of $ZnCl_2$ by KOH. In the control, the direct carbonized sample was denoted as B-800. In another control, the commonly-used hydrothermal method was conducted at 180 °C for 6 h (the obtained sample was referred to as HT-B).

Characterization: Transmission electron microscopy (TEM) was carried out with a JEM-2000 FX instrument operating at a 200 kV accelerating voltage. Scanning electron microscopy (SEM) images were taken using a Philips XL 30 instrument and a JEOL JSM-6700F microscope. Energy dispersive X-ray analysis (EDX) was done on the same instrument. The X-ray photoelectron spectroscopy (XPS) was measured with an ESCALAB 250 (Thermo Electron). The X-ray excitation was provided by a monochromatic Al Kα (1486.6 eV) source. Survey scans were obtained using a pass energy of 100 eV while high resolution scans of specific elements were obtained using a 20 eV pass energy. The detection of the emitted photoelectrons was performed perpendicular to the surface sample. Data quantification was performed on the Avantage program. The surface atomic concentrations were determined from photoelectron peaks areas using the atomic sensitivity factors reported by Scofield. Binding energies (BE) of all core levels were referred to the C–C bond of C1s at 284.6 eV. In addition, elemental analysis was performed on a Vario EL cube (Elementar Analysensysteme GmbH) to determine the carbon, nitrogen and hydrogen contents of the samples. Nitrogen sorption isotherms were measured at 77 K with a Quadrachrome adsorption instrument. Before analysis, the samples were degassed at 200 °C for 24 h (except for bacteria (B) which was degassed at 100 °C for 36 h). The surface area was calculated using the BET method based on adsorption data in the relative pressure (P/P_0) range of 0.06 to 0.14 and the total pore volume was determined from the amount of nitrogen adsorbed at a relative pressure (P/P_0) of 0.99. The pore size distribution (PSD) was determined via a nonlocal density functional theory (NLDFT) method using nitrogen adsorption data, and assuming a slit pore model.

Electrochemical Measurements: ORR measurements were conducted using cyclic voltammetry and linear sweep voltammetry measurements in a three-electrode system. A glassy carbon rotating ring-disk electrode (RDE, Pine Instruments Co.) was used as the working electrode. An Ag/AgCl electrode was used as the reference electrode and Pt wire was used as the counter electrode. The working electrode was prepared by loading a catalyst suspension (1.0 mg/mL in ethanol, 20 μg) onto the surface of glassy carbon disk (5 mm), followed by drying at room temperature. After air-drying, the electrode was covered with Nafion (0.05 wt%). The cyclic voltammetry experiments were performed in oxygen-saturated 0.1 M KOH solution with a scan rate of 100 mV s^{-1}. RDE and RRDE measurements were carried out on a MSRX speed controller (Pine Instruments Co.) and a CHI400 (CHI INC. Austin) bipotentiostat.

Electron transfer numbers were calculated using the Koutecky–Levich equation:

$$1/J = 1/J_K + 1/J_L = 1/(nFkGC_0) + 1/(0.620nFAD_{O2}^{2/3}\omega^{1/2}\upsilon^{-1/6}C_0) = 1/(nFkGC_0) + 1/(B\omega^{1/2})$$

where, J is the measured current density; J_K and J_L are the kinetic- and diffusion-limiting current densities; n is the number of electrons exchanged per mole of O_2; F is the Faraday constant (96 500 C mol^{-1}); Γ is the quantity of catalyst on the surface of the electrode (mol cm^{-2}); k is the rate constant for oxygen reduction; A is electrode area (cm^2); C_0 is bulk concentration of O_2 in (1.2×10^{-6} mol cm^{-3}); D_{O2} is the diffusion coefficient of O_2 in solution (1.9×10^{-5} cm^2 s^{-1}); ω is the rotation rate (rad s^{-1}) and υ is the kinetic viscosity of the water (0.01 cm^2 s^{-1}).

In the RRDE experiments, the transferred electron number (n) per oxygen molecule was calculated from: $n = 4I_D/(I_D + I_R/N)$ Here, I_D and I_R stand for the disk and ring currents, respectively, and N is the ring collection efficiency. The ring collection efficiency was independently determined using 10 mM ferricyanide ($K_3[Fe(CN)_6]$) in 0.1 M KCl solution. The measured N value was 0.27.

Capacitance Measurements: The working electrode was prepared by mixing an active material (85 wt%) with acetylene black (10 wt%) and poly(vinylidene difluoride) (PVDF) (5 wt%) in N-methylpyrrolidone. The slurry was coated on a piece of stainless collector with pressure. The three-electrode configuration was used to evaluate the electrocapacitive performance. In the three-electrode system, a Pt foil was applied as the counter electrode. The galvanostatic measurement was performed by a Land cell tester (Wuhan, China) with different current densities.

Supporting Information

Supporting Information is available from the Wiley Online Library or from the author.

Acknowledgements

This work was supported by the National Natural Science Foundation of China (No. 20890022) and the National Key Basic Research Development Project of China (No. 2010CB933602).

Received: June 18, 2012
Revised: July 13, 2012
Published online: October 12, 2012

[1] a) C. D. Liang, Z. J. Li, S. Dai, *Angew. Chem. Int. Ed.* **2008**, *47*, 3696; b) Y. G. Guo, J. S. Hu, L. J. Wan, *Adv. Mater.* **2008**, *20*, 2878.
[2] Z. W. Chen, D. Higgins, A. P. Yu, L. Zhang, J. J. Zhang, *Energy Environ. Sci.* **2011**, *4*, 3167.
[3] a) M. Inagakia, H. Konnoa, O. Tanaike, *J. Power Sources* **2010**, *195*, 7880; b) S. R. S. Prabaharan, R. Vimala, Z. Zainal, *J. Power Sources* **2006**, *161*, 730.
[4] a) K. P. Gong, F. Du, Z. H. Xia, M. Durstock, L. M. Dai, *Science* **2009**, *323*, 760; b) D. S. Yu, Q. Zhang, L. M. Dai, *J. Am. Chem. Soc.* **2010**, *132*, 15127; c) J. W. Gallaway, S. A. C. Barton, *J. Am. Chem. Soc.* **2008**, *130*, 8527. d) B. L. Allen, P. D. Kichambare, A. Star, *ACS Nano* **2008**, *2*, 1914.
[5] X. Q. Wang, J. S. Lee, Q. Zhu, J. Liu, Y. Wang, S. Dai, *Chem. Mater.* **2010**, *22*, 2178.
[6] a) W. Yang, T. P. Fellinger, M. Antonietti, *J. Am. Chem. Soc.* **2011**, *133*, 206; b) G. Wu, K. L. More, C. M. Johnston, P. Zelenay, *Science* **2011**, *332*, 443; c) R. L. Liu, D. Q. Wu, X. L. Feng, K. Mullen, *Angew. Chem. Int. Ed.* **2010**, *49*, 2565.
[7] a) Z. H. Sheng, L. Shao, J. J. Chen, W. J. Bao, F. B. Wang, X. H. Xia, *ACS Nano* **2011**, *5*, 4350; b) R. B. Hye, S. Jin, S. H. Yang, *Chem.*

Mater. **2011**, *23*, 3421; c) S. B. Yang, X. L. Feng, X. C. Wang, K. Mullen, *Angew. Chem. Int. Ed.* **2011**, *50*, 5339.

[8] a) C. X. Guo, H. B. Yang, Z. M. Sheng, Z. S. Lu, Q. L. Song, C. M. Li, *Angew. Chem. Int. Ed.* **2010**, *49*, 3014; b) C. X. Guo, X. T. Zheng, Z. S. Lu, X. W. Lou, C. M. Li, *Adv. Mater.* **2010**, *22*, 5164; c) C. X. Guo, Y. Q. Shen, Z. L. Dong, X. D. Chen, X. W. Lou, C. M. Li, *Energy Environ. Sci.* **2012**, *5*, 6919.

[9] a) Y. J. Kim, Y. Abe, T. Yanagiura, K. C. Park, M. Shimizu, T. Iwazaki, S. Nakagawa, M. Endo, M. S. Dresselhaus, *Carbon* **2007**, *45*, 2116; b) R. J. White, M. Antonietti, M. M. Titirici, *J. Mater. Chem.* **2009**, *19*, 8645; c) L. Zhao, L. Z. Fan, M. Q. Zhou, H. Guan, S. Qiao, M. Antonietti, M. M. Titirici, *Adv. Mater.* **2010**, *22*, 5202.

[10] a) H. Zhu, X. L. Wang, F. Yang, X. R. Yang, *Adv. Mater.* **2011**, *23*, 2745; b) L. Wei, M. Sevilla, A. B. Fuertes, R. Mokaya, G. Yushin, *Adv. Energy Mater.* **2011**, *1*, 356.

[11] J. Nicklin, K. Graeme-Cook, R. Killington, *Instant Notes in Microbiology*, BIOS Scientific Publishers Ltd., Berkshire, UK **2002**.

[12] M. M. Nakano, P. Zuber, *Annu. Rev. Microbiol.* **1998**, *52*, 165.

[13] a) P. Kuhn, A. Forget, D. Su, A. Thomas, M. Antonietti, *J. Am. Chem. Soc.* **2008**, *130*, 13333; b) W. Zhang, C. Li, Y. P. Yuan, L. G. Qiu, A. J. Xie, Y. H. Shen, J. F. Zhu, *J. Mater. Chem.* **2010**, *20*, 6413.

[14] a) T. E. Rufford, D. Hulicova-Jurcakova, K. Khosla, Z. Zhu, G. Q. Lu. *J. Power Sources* **2010**, *195*, 912; b) T. E. Rufford, D. Hulicova-Jurcakova, E. Fiset, Z. Zhu, G. Q. Lu, *Electrochem. Commun.* **2009**, *11*, 974.

[15] a) M. Molina-Sabio, F. Rodríguez-Reinoso, *Colloids Surf., A* **2004**, *241*, 15; b) F. Rodríguez-Reinoso, M. Molina-Sabio, *Carbon* **1992**, *30*, 1111.

[16] a) W. M. Li, A. P. Yu, D. C. Higgins, B. G. Llanos, Z. W. Chen, *J. Am. Chem. Soc.* **2010**, *132*, 17056; b) D. S. Yu, E. Nagelli, F. Du, L. M. Dai, *J. Phys. Chem. Lett.* **2010**, *1*, 2165; c) W. Yang, Y. Wang, J. Li, X. R. Yang, *Energy Environ. Sci.* **2010**, *3*, 144; d) W. Yang, X. L. Wang, F. Yang, C. Cheng, X. R. Yang, *Adv. Mater.* **2008**, *20*, 2579.

[17] A. J. Bard, L. R. Faulkner, *Electrochemical Methods: Fundamentals and Applications*, John Wiley & Sons, New York **2001**.

[18] J. F. Moulder, W. F. Stickle, P. E. Sobel, K. D. Bomben, *Handbook of X-Ray Photoelectron Spectroscopy - A Reference Book of Standard Spectra for Identification and Interpretation of XPS Data*, Perkin-Elmer Corporation, Eden Prairie, MN, USA **1992**.

[19] a) B. E. Conway, *Electrochemical Supercapacitors*, Kluwer Academic/ Plenum Publishers, New York **1 999**; b) P. Simon, Y. Gogotsi, *Nat. Mater.* **2008**, *7*, 845.

[20] a) C. X. Guo, C. M. Li, *Energy Environ. Sci.* **2011**, *4*, 4504; b) C. X. Guo, M. Wang, T. Chen, X. W. Lou, C. M. Li*Adv. Energy Mater.* **2011**, *1*, 448.

[21] a) D. Hulicova, M. Kodama, H. Hatori, *Chem. Mater.* **2006**, *18*, 2318. b) H. Guo, Q. Gao, *J. Power Sources* **2009**, *186*, 551.

[22] a) J. Chmiola, G. Yushin, Y. Gogotsi, C. Portet, P. Simon, P. L. Taberna, *Science* **2006**, *313*, 1760; b) E. Raymundo-Piñero, K. Kierzek, J. Machnikowski, F. Béguin, *Carbon* **2006**, *44*, 2498.

[23] a) C. Zheng, L. Qi, M. Yoshio, H. Y. Wang, *J. Power Sources* **2010**, *195*, 4406; b) A. G. Pandolfo, A. F. Hollenkamp, *J. Power Sources* **2006**, *157*, 11.